

Theoretical Bounds on the Estimation of Transverse Displacement, Transverse Strain and Poisson's Ratio in Elastography

ELISA E. KONOFAGOU, TOMY VARGHESE AND JONATHAN OPHIR

*Ultrasonics Laboratory
Department of Radiology
University of Texas Medical School
Houston, TX 77030
Email: elisak@bwh.harvard.edu*

The Cramér-Rao Lower Bounds (CRLB) are derived for the displacement and strain estimation in directions orthogonal to the ultrasonic beam axis, using a previously-described recorelation method of axial, lateral and elevational motion estimation. We also compare it to the lateral tracking method that involves the sole use of the axial signal in the transverse direction. Our theoretical results, verified with simulations and phantom experiments, show that elastography is capable of measuring axial and transverse strain at up to 10% axially applied compression. Finally, we predict the performance of the estimation of the Poisson's ratio using decoupled axial and lateral estimates that result from the recorelation method.

KEY WORDS: Axial; decoupling; displacement; elastography; lateral; orthogonal; Poisson's ratio; recorelation; strain; Strain Filter; transverse; ultrasound.

1. INTRODUCTION

Elastography is an imaging technique that depicts the local strain experienced by the ultrasonically-scanned tissue under a static compression. Most commonly, tissue strain is estimated in the axial direction; i.e., parallel to the ultrasonic beam symmetry axis, which is also the direction of the applied compression. The axial tissue strain is computed by taking the gradient of the axial displacement that occurred due to the applied compression. The axial displacement is estimated by using cross-correlation techniques to compute the lag between pre- and postcompression ultrasonic signals.¹ Therefore, in its current practice, elastography estimates strain in one direction only, while assuming that strains in all other directions are comparatively small and, therefore, negligible. However, Kallel et al.² have shown theoretically and experimentally that this assumption may lead to major estimation errors, especially in the case of relatively larger strains.

These errors are due to the fact that the estimation of strain in tissues under compression is in reality a three-dimensional problem, i.e., the three orthogonal strain components are not separable if the tissue is incompressible. Therefore, the estimation of one strain component, as is the case in elastography, is corrupted by decorrelation noise due to motion in an orthogonal direction. Corrections should, therefore, be performed in order to reduce these errors. In fact, the coupling coefficient between strains in orthogonal directions is described by a mechanical parameter, the Poisson's ratio (defined as the ratio of two orthogonal strain components).

Recently, Konofagou and Ophir³ developed a method that combines cross-correlation and interpolation to first estimate lateral displacement and strain with high signal-to-noise ratio, and then use those displacement estimates to correct the strain estimation in an orthogonal direction. First, the postcompression rf sonogram undergoes global stretching by the amount

of axial compression applied, in order to increase the correlation (or, achieve a recorelation) of the initial precompression with the corrected postcompression rf sonogram.⁴ Then, the lateral displacement is estimated using an interpolation technique to overcome the interbeam spacing (or, pitch) limitation imposed by the transducer characteristics, and crosscorrelation (in the transverse direction) of the short precompression with the stretched postcompression axial rf segments. The resulting high precision lateral displacement is then used to (a) estimate the lateral strain and (b) shift the postcompression rf segments in the (opposite) lateral direction by the amount of estimated displacement. The latter step also achieves recorelation of the segments by reducing decorrelation due to lateral motion. The axial strain is then estimated by using the initial pre- with the corrected postcompression sonogram. The same principle can be applied in a 3D setting, where correction for the axial motion for all transverse (or, orthogonal to the axial direction) motion estimation is applied and vice versa.⁵

This method is called the ‘recorelation method’ because it achieves an increase of the axial and lateral correlation coefficients (or, *axial* and *lateral recorelation*, respectively) through correction for the corresponding motions. This technique assumes the use of a single transducer/compressor unit and makes no assumptions regarding the compressibility properties of the tissue. Furthermore, the use of interpolation overcomes the transducer element pitch limitation and provides high precision lateral displacement estimates. Kallel et al² have shown that the correlation coefficient between echo segments depends on the scaling of the signal in the axial direction due to strain and the displacement in the lateral direction. Therefore, this correction method uses temporal stretching in the axial direction⁴⁶ and corrects for lateral motion³ to compensate for lateral decorrelation. Finally, the local Poisson’s ratio is estimated using decoupled axial and lateral estimates.

Most ultrasound-related papers dealing with the biomechanical properties of tissues and, more precisely, the reconstruction of the elastic modulus⁷⁻¹⁰ have assumed that all tissues are incompressible, with a constant Poisson’s ratio very close to 0.5. However, some pathological tissues such as edematous muscle tissues,¹¹ lung tissue¹² ($\nu = 0.3$) and cartilage¹³ ($\nu = 0.18$) have been shown to have lower Poisson’s ratios and thus the simple a-priori assumption of incompressibility^{8,10} may result in erroneous imaging of the elastic modulus. Therefore, mapping the Poisson’s ratio in tissues serves a double purpose: it can help (a) verify the theoretical assumption and (b) detect anisotropic, viscoelastic and/or poroelastic tissues with a multitude of applications in the meat industry, tissue engineering and edema treatment monitoring⁵.

Previously-developed the theory for lateral motion estimation involved either the use of the lateral envelope^{14,16} or a 2D kernel¹⁵ in the estimation of lateral motion. Bonnefous¹⁷ first introduced a method for using the 1-D axial information for 1-D lateral tracking and applied it to flow measurements. In this paper, we investigate the theoretical limits involved in the strain estimation in a nonaxial direction as measured using the aforementioned method³ while comparing it to the alternative of using the lateral envelope. The former involves the use of the axial phase in the lateral direction after compensation for axial distortion, while the latter considers the use of lateral envelope for motion estimation, i.e., the absence of axial phase. Throughout this paper, the theory is developed for lateral estimation but it can be used to encompass estimation in any transverse direction.

In elastography, the strain filter⁸ serves both as a theoretical framework and a prediction tool for axial strain estimation. The strain filter shows that the estimation of low strains is mainly corrupted by random noise, while the estimation of higher strains is limited by decorrelation noise due to both axial and nonaxial motion. In this study, we develop similar theoretical prediction tools that will show the theoretical relationship between several parameters: (1) ultrasonic parameters, such as the beamwidth, the interelement spacing (or pitch) and the center frequency; (2) signal processing parameters, such as the number of in-

terpolates; and (3) mechanical parameters, such as the Poisson's ratio. Together they determine the estimation of transverse displacements and strains. Finally, we develop optimization criteria based on these theoretical predictions.

2. THEORY

In a 2D scanning model with a 1D transducer, the point-spread function (psf) may be written as a separable function in the focal area,¹⁶ viz.

$$p(x, y) = p_a(x)p_l(y) \quad (1)$$

where x and y are the axial and lateral coordinates, respectively, and $p_a(x)$ and $p_l(y)$ are the axial and lateral psf components, respectively. If we assume a Gaussian modulated emitted pulse, the axial psf component becomes

$$p_a(x) = Ae^{-\frac{x^2}{2\sigma_x^2}} \cos\left(2\pi \frac{x}{\lambda}\right) \quad (2)$$

and the lateral psf component of an unapodized, box car transducer aperture (not considering grating lobes) is¹⁹

$$p_l(y) = \left(\frac{\sin\left[\frac{\pi Dy}{\lambda x_r}\right]}{\left[\frac{\pi Dy}{\lambda x_r}\right]} \right)^2 = \left(\frac{\sin\left[\frac{\pi y}{\lambda F}\right]}{\left[\frac{\pi y}{\lambda F}\right]} \right)^2 \quad (3)$$

where x is the axial coordinate, σ_x is the pulse length in mm, λ is the central wavelength of the emitted pulse, D is the azimuthal aperture width, y is the lateral coordinate, x_r is the focal length and F is the F-number of the transducer given by

$$F = \frac{x_r}{D} \quad (4)$$

Using this theoretical model, we evaluate the fundamental limits on estimation of the lateral displacement, lateral strain and Poisson's ratio. In the case of lateral motion estimation, we consider two 1-D cases. First, the case where the lateral envelope is used for lateral tracking and second, the case where the axial signal is used in the lateral direction for motion estimation in the same direction.

A. Theoretical bounds on the estimation of lateral displacement and lateral strain

1. Using the axial signal

In this section, we develop the theory that describes the use of 1D axial signal in formation for 1D lateral displacement, strain estimation and recorelation and then contrast it with the

performance of the lateral envelope method previously described. The lateral strain is defined as the gradient of the lateral displacement, i.e.,

$$\hat{\varepsilon}_l = \frac{\hat{\tau}_{l2} - \hat{\tau}_{l1}}{\Delta b} \quad (5)$$

where $\hat{\tau}_{l1}$ and $\hat{\tau}_{l2}$ are two lateral displacement estimates (or, lateral shifts) computed by crosscorrelating pre- and postcompressed rf (axial) segments (separated by a lateral distance Δb , which in this case is equal to the pitch). In appendix A, based on the derivation by Zagar et al.,²⁰ we show the following expression linking the normalized standard error in the estimation of the cross-correlation function ($R_{l2}(\tau)$) to the variance of the estimate of the shift τ , $\sigma^2(\hat{\tau})$,

$$\varepsilon^2 [\hat{R}_{l2}(\tau)] \cong \left(2 \frac{(\pi B)^2 + 3(\pi f_0)^2}{\sqrt{3}} \right)^2 \sigma^4(\hat{\tau}) \quad (6)$$

where B is the bandwidth, f_0 is the center frequency of the transmitted pulse and $\hat{\tau}$ is the estimated time delay. Eq. (6) is the first term of a Taylor expansion approximation and was derived under the valid assumptions that the precompressed and postcompressed signals have a Gaussian amplitude distribution and that both in the integration time and the time-bandwidth product are sufficiently large, i.e., $T \geq 10|\tau|$ and $BT \geq 5$, where T is the window size. Throughout this section, $\hat{\cdot}$ denotes the estimated value of a parameter and its absence denotes the true value of the same parameter.

By definition of the normalized standard error ε , we have²¹

$$\varepsilon^2 [\hat{R}_{l2}(\tau)] = \frac{\sigma^2 [\hat{R}_{l2}(\tau)]}{R_{l2}^2(\tau)} \quad (7)$$

$$\begin{aligned} &= A \frac{\sigma^2 [\hat{\rho}_{l2}(\tau)]}{\rho_{l2}^2(\tau)} \\ &= A \varepsilon^2 [\hat{\rho}_{l2}(\tau)] \end{aligned} \quad (8)$$

where A is an assumed constant of proportionality between the errors in the estimations of the crosscorrelation function and correlation coefficient, and ρ_{l2} is the correlation coefficient given by

$$\rho_{l2}(\tau) = \frac{R_{l2}(\tau)}{\sqrt{R_{l1}(0)R_{l2}(0)}} \quad (9)$$

and $R_{l1}(0)$ and $R_{l2}(0)$ are equal to the autocorrelations at $\tau = 0$ of pre- and postcompressed signals, respectively. From Eqs. (6), (7) and (8) we obtain

$$\sigma^2 [\hat{\rho}_{12}(\tau)] \cong \frac{I}{A} \left(2 \frac{(\pi B)^2 + 3(\pi f_0)^2}{\sqrt{3}} \right)^2 \sigma^4(\hat{\tau}) \rho_{12}^2(\tau) \quad (10)$$

However, since we are estimating the peak of the cross-correlation coefficient, the true correlation coefficient is one, i.e., $\rho_{12}^2(\tau) = 1$ (where τ is the lag, at which ρ_{12}^2 is maximum) and, therefore, Eq. (10) becomes

$$\sigma^2 [\hat{\rho}_{12}(\tau)] \cong \frac{I}{A} \left(2 \frac{(\pi B)^2 + 3(\pi f_0)^2}{\sqrt{3}} \right)^2 \sigma^4(\hat{\tau}) \quad (11)$$

Both the axial displacement estimation and the lateral tracking methods use the correlation coefficient of the axial signal, $\rho_{12} = \hat{\rho}$, to estimate the axial shift ($\hat{\tau}_a$) and lateral shift ($\hat{\tau}_l$). Therefore, Eq. (11) becomes

$$\frac{I}{A} \left(2 \frac{(\pi B_l)^2 + 3(\pi f_{0l})^2}{\sqrt{3}} \right)^2 \sigma^4(\hat{\tau}_l) = \frac{I}{A} \left(2 \frac{(\pi B_a)^2 + 3(\pi f_{0a})^2}{\sqrt{3}} \right)^2 \sigma^4(\hat{\tau}_a) \quad (12)$$

or,

$$\begin{aligned} \sigma^4(\hat{\tau}_l) &= \left(\frac{B_a^2 + 3f_{0a}^2}{B_l^2 + 3f_{0l}^2} \right)^2 \sigma^4(\hat{\tau}_a) \\ &= \left(\frac{B_a^2 + 3f_{0a}^2}{B_l^2} \right)^2 \sigma^4(\hat{\tau}_a) \end{aligned}$$

since for the band width and center frequency of the lateral PSF, we have, respectively, $B_l \cong 1/b$, where b is the band width, and $f_{0l} = 0$ (see Eq. (A.1)). We then find the relationship between the standard deviation of the lateral shift estimate and the standard deviation of the axial shift estimate to be

$$\sigma(\hat{\tau}_l) = Bb \sqrt{1 + \frac{3}{b_l^2}} \sigma(\hat{\tau}_a) \quad (13)$$

or

$$\sigma(\hat{\tau}_l) \approx \frac{b}{l_p} \sqrt{1 + \frac{3}{b_l^2}} \sigma(\hat{\tau}_a)$$

where l_p denotes the pulsewidth or range gate size ($\equiv l/b$), $B = B_a$ and b_l is the fractional bandwidth ($=B_a/f_a$). Eq. (13) can also be written as follows

$$\frac{\sigma(\hat{\tau}_l)}{\sigma(\hat{\tau}_a)} \approx A_l \left(\frac{b}{l_p} \right) \quad (14)$$

where $A_l = \sqrt{1 + 3/b_l^2}$. Eq. (14) is very important in the sense that it shows that the estimation of the lateral versus the axial shift (or, displacement) is related to the ratio of the lateral to the axial ultrasonic resolution (assumed equal to the pulsewidth). In other words, the closer the lateral resolution to the axial resolution, the more comparable the two estimations become. In a typical ultrasound system setting, we have $b_l = 0.6$ (60% relative bandwidth), a beamwidth equal to 1 mm and a range gate size also equal to 1 mm.²² In that case, $\sigma(\hat{\tau}_l) \cong 3\sigma(\hat{\tau}_a)$. In a more preferred setting, the relative bandwidth is 100% and then $\sigma(\hat{\tau}_l) \cong 2\sigma(\hat{\tau}_a)$. The additional advantage of increasing the relative bandwidth is the fact that the estimation of the time shift further improves.⁸ However, although Eq. (14) implies that the axial and lateral shifts can be estimated at comparable precision, the lateral shift estimation should be more corrupted by estimation noise. The fundamental principle behind this comparable precision is that the correlation coefficients describing the estimation of axial and lateral motion are equal (see figure 9) and this is achieved only when motions are decoupled and corrected for, i.e., with the recorrelation method.

In order to determine the Lateral Strain Filter (LSF), which describes the estimation of the lateral strain from the lateral shifts, or displacement, estimates, we need to associate the variance of the lateral strain to that of the lateral displacement of Eq. (12). From Eq. (1), the variance of the strain estimate is given by

$$\sigma^2(\hat{\epsilon}_l) = \frac{\sigma^2(\hat{\tau}_{l1}) + \sigma^2(\hat{\tau}_{l2}) - 2\text{cov}(\hat{\tau}_{l1}, \hat{\tau}_{l2})}{\Delta b^2} \quad (15)$$

The van Cittert-Zernike theorem^{23,24} predicts that for two points in a nonapodized, rectangular array with common transmit and receive elements, the correlation coefficient of the speckle echo data received at the two elements at a distance Δb and since the two lateral shift estimates are also taken at the same distance Δb apart, is given by

$$\rho_{\hat{\tau}_{l1}, \hat{\tau}_{l2}} \approx \left(1 - \frac{\Delta b}{b} \right) \quad (16)$$

where b is the -6 dB beamwidth. Since

$$\text{cov}(\hat{\tau}_{l1}, \hat{\tau}_{l2}) = \rho_{\hat{\tau}_{l1}, \hat{\tau}_{l2}} \sigma(\hat{\tau}_{l1}) \sigma(\hat{\tau}_{l2}) \quad (17)$$

by assuming that

$$\sigma(\hat{\tau}_l) = \sigma(\hat{\tau}_{l1}) = \sigma(\hat{\tau}_{l2}) \quad (18)$$

we obtain from Eqs. (15), (16), (17) and (18)

$$\begin{aligned}\sigma^2(\hat{\epsilon}_l) &= \frac{2\sigma^2(\hat{\tau}_l) - 2\sigma^2(\hat{\tau}_l)\left(1 - \frac{\Delta b}{b}\right)}{\Delta b^2} \\ &= \frac{2\sigma^2(\hat{\tau}_l)}{\Delta b^2} \left(1 - \left(1 - \frac{\Delta b}{b}\right)\right) \\ &= \frac{2\sigma^2(\hat{\tau}_l)}{b\Delta b}\end{aligned}$$

which is similar to the result in the case of the axial strain estimation variance derived by Céspedes et al.²⁵

The lower bound of $\sigma(\hat{\tau}_l)$ is given by the Ziv-Zakai lower bound⁸, i.e.,

$$\sigma^2(\hat{\tau}_l)_{ZLLB} = \begin{cases} \frac{3}{2\pi^2 T (B^3 + 12Bf_0^2)} \left[\frac{1}{\rho^2} \left(1 + \frac{1}{SNR_S^2}\right)^2 - 1 \right], & \eta < BTSNR_C \\ \frac{18}{\pi^2 T \left(\frac{B^5}{f_0^2} + 12B^3\right)} \left[\frac{1}{\rho^2} \left(1 + \frac{1}{SNR_S^2}\right)^2 - 1 \right], & \gamma < BTSNR_C < \eta \\ \frac{(\epsilon T)^2}{12}, & , BTSNR_C < \gamma \end{cases} \quad (20)$$

The upper bound on the signal-to-noise ratio in the lateral strain estimation is defined by

$$SNR_e^{UB} = \frac{\overline{\hat{\epsilon}_l}}{\sigma(\hat{\epsilon}_l)_{ZLLB}} \quad (21)$$

where $\overline{\hat{\epsilon}_l}$ is the mean lateral strain estimate, and, in combination with Eqs. (13) and (21), leads to the Lateral Strain Filter (LSF) for mula expressed by

$$SNR_e^{UB} = \begin{cases} \pi \bar{\epsilon}_l \sqrt{\frac{T \Delta b (B^3 + 12 B f_0^2)}{3b (B^2 + 3 f_0^2) \left[\frac{1}{\rho^2} \left(1 + \frac{1}{SNR_S^2} \right)^2 - 1 \right]}}, & \eta < BTSNR_C \\ \pi \bar{\epsilon}_l \sqrt{\frac{T \Delta b \left(\frac{B^5}{f_0^2} + 12 B^3 \right)}{18b (B^2 + 3 f_0^2) \left[\frac{1}{\rho^2} \left(1 + \frac{1}{SNR_S^2} \right)^2 - 1 \right]}}, & \gamma < BTSNR_C < \eta \\ \frac{12}{T} \sqrt{\frac{\Delta b}{2b (B^2 + 3 f_0^2)}}, & , BTSNR_C < \gamma \end{cases} \quad (22)$$

where SNR_s and SNR_c are the sonographic and composite signal-to-noise ratios,¹⁸ respectively and η and γ are the threshold limits.¹⁸ The reader should note that the correlation coefficient ρ is the same in both the Axial Strain Filter (ASF) and Lateral Strain Filter (LSF) and is given by

$$\rho = \rho_a \rho_l, \quad (23)$$

where ρ_a is the axial correlation coefficient given by Eq. (2) (we assume that the psf can be characterized by the autocorrelation function and vice versa) and ρ_l is the lateral correlation coefficient given by Eq. (3) and

$$\rho_l(x_0) \approx \exp\left(-A \frac{(-v \epsilon_a x_0)^2}{b^2}\right)$$

or

$$\rho_l(x - \hat{x}) \approx \exp\left(-A \frac{(-v \epsilon_a (x - \hat{x}))^2}{b^2}\right) \quad (24)$$

where x and \hat{x} are the true and estimated lateral correlation peak positions, respectively, and A is a constant that adjusts for the beam level, where the beam width is measured, and the sinc-to-Gaussian equivalence.²⁵ Interpolation techniques are used to better estimate the true peak due to the scarce lateral sampling. In other words, the distance between the true and estimated correlation peak is reduced with the number of interpolates. This translates to the fact that the effective pitch is also reduced due to the interpolation. Eq. (24) then becomes

$$\rho_l \approx \exp\left(-A \frac{\left(-v\varepsilon_a \frac{\Delta b}{N}\right)^2}{b^2}\right)$$

or

$$\rho_l = \exp\left(-A \left(\frac{-v\varepsilon_a \Delta b}{Nb}\right)^2\right) \quad (25)$$

where Δb is the original pitch of adjacent A-lines (as defined by the ultrasonic system) and N denotes the number of interpolates. From Eqs. (22) and (25) it is important to note that the LSF depends on the pitch-to-beamwidth ratio; the higher the pitch-to-beamwidth ratio (or, equivalently, the lower the beam overlap), the higher the area under the SF and, therefore, the better the performance of the estimator (Figs. 1, 2).

From Eq. (22) we can deduce that the parameters affecting the estimation of strain in the lateral direction are the beam width (Fig. 1), in ter po la tion (Fig. 2), pitch (Fig. 3), band width (Fig. 4), center frequency (Fig. 5a) and sonographic signal-to-noise ratio (Fig. 5b). From Figs. (1)-(5), we conclude that the optimal conditions for lateral strain estimation are high center frequency, large band width, fine beam width (low beam overlap), high sonographic signal-to-noise ratio, large pitch and intensive interpolation. The reader should note that the beam width and the center frequency are not independent. Except when otherwise indicated, figures (1) to (5) were generated using 5 MHz center frequency, 50% fractional band width, 1 mm beam width, 0.4 mm pitch, a 1000:1 in ter po la tion scheme and 40 dB sonographic signal-to-noise ratio. The ultrasonic parameters were chosen to match those of our experimental setup using a real-time linear array scanner (Diasonics Spectra II, Santa Clara, CA, USA).

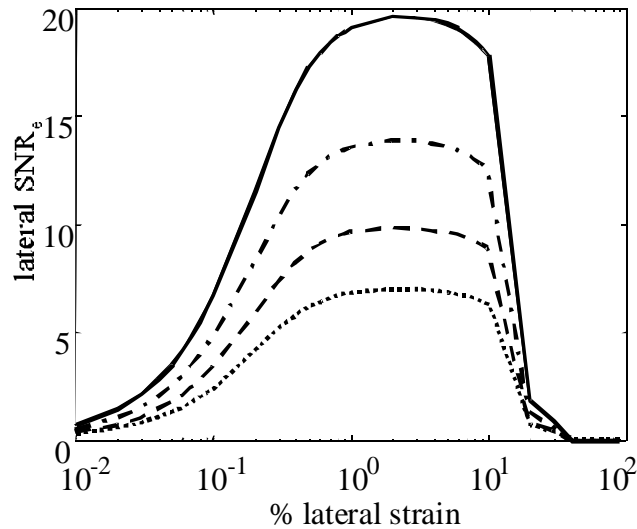


FIG. 1 Dependence on the beamwidth (mm): 1 (solid), 2 (-.-), 3 (---), 4 (.), corresponding to overlaps of 60%, 70%, 80% and 90%, respectively.

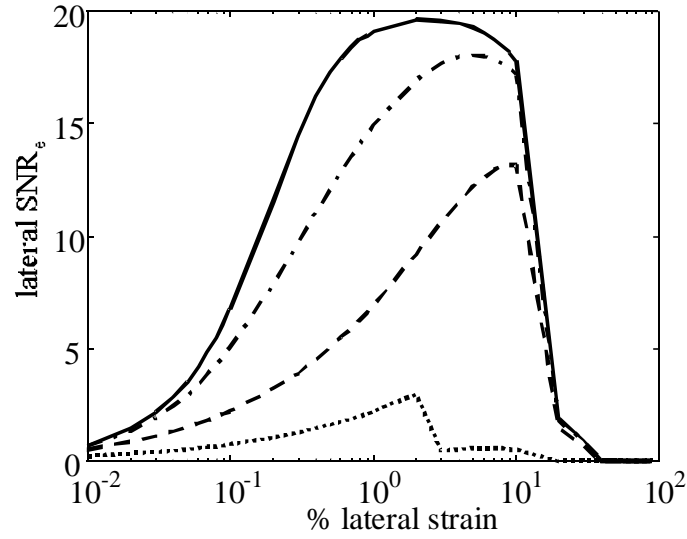


FIG. 2 Dependence on interpolation scheme: 1:1 (· · ·), 10:1 (—), 100:1 (---), 1000:1 (solid).

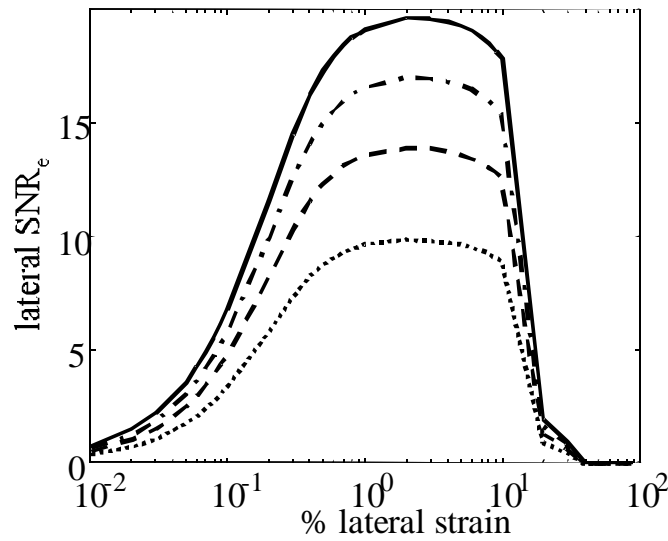


FIG. 3 Dependence on pitch (mm): 0.4 (solid), 0.3 (---), 0.2 (— · —), 0.1 (· · ·) corresponding to overlaps of 60%, 70%, 80% and 90%, respectively.

2. Using the lateral envelope

A straightforward lateral tracking method, whose performance has been predicted in the literature,^{14,15} uses the lateral envelope to estimate motion in the lateral direction. Below we derive the theoretical result for this method in its application of lateral strain estimation. Lateral strain ($\hat{\epsilon}_l$) is the displacement gradient, which is estimated from two adjacent displacement estimates separated by a spatial interval (Δx), viz.

$$\hat{\epsilon}_l = \frac{\hat{d}_2 - \hat{d}_1}{\Delta x} \quad (26)$$

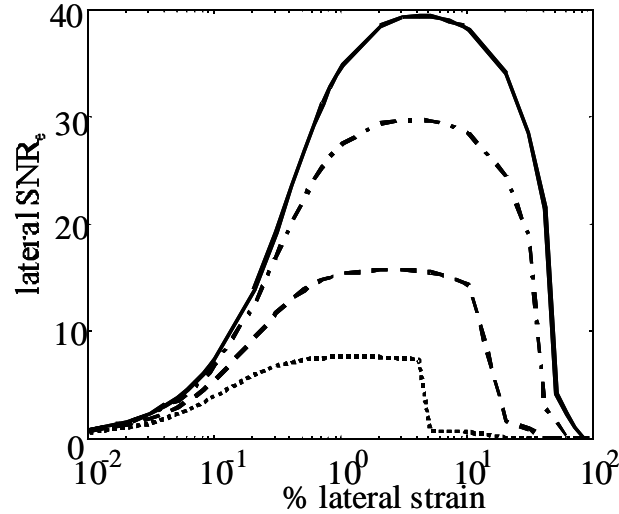


FIG. 4 Dependence on relative bandwidth: 30% (.), 50% (---), 60% (-.-) and 80% (solid).

where \hat{d}_1 is the displacement estimate at lateral distance x , and \hat{d}_2 is the Cramér-Rao Lower Bound (CRLB) displacement estimate at lateral distance $x + \Delta x$. The reader should note that although the parameter being estimated is also the lateral displacement, we choose to refer to it in this section by ' d ' in stead of ' τ ' to emphasize the fact that in the former case, the lateral envelope in stead of the axial signal is used. Since the strain estimate is obtained from a linear combination of two random variables (displacement estimates separated by Δx), the variance of the strain estimator depends on the variance of the displacement estimator. Assuming that the echo signal is stationary, the lower bound on the variance of the strain estimate (σ_ϵ^2) is expressed in terms of the lower bound on the variance of the displacement estimates (σ_d^2) in Céspedes et al.⁵, and is given by

$$\sigma_\epsilon^2 \geq \frac{2\sigma_d^2}{x\Delta x} \quad (27)$$

where x is the length of the cross-correlation window and the displacement variance is given by (as shown in appendix B)

$$\sigma_{d,CRLB,\rho}^2 \geq \frac{3c}{2\pi^2 \chi f_{om}^3} \left[\frac{1}{\rho^2} \left(1 + \frac{1}{SNR^2} \right)^2 - 1 \right] \quad (28)$$

where f_{om} denotes the maximum frequency of the spectrum of the lateral PSF, and c is the speed of sound. Eq. (27) illustrates that for a given window length (x) and overlap (Δx), the strain variance is reduced when the variance in the displacement estimate is minimized. Figure 6 shows the advantages of lateral tracking using the rf signal in stead of the lateral envelope. It compares the theoretical upper bounds on the signal-to-noise ratio using the lateral envelope versus the rf signal and shows an order of magnitude improvement using the latter. The lateral envelope result corroborates other theoretical results reported in the literature on the poor performance of lateral tracking estimation using the lateral envelope.¹⁴⁻¹⁶ However,

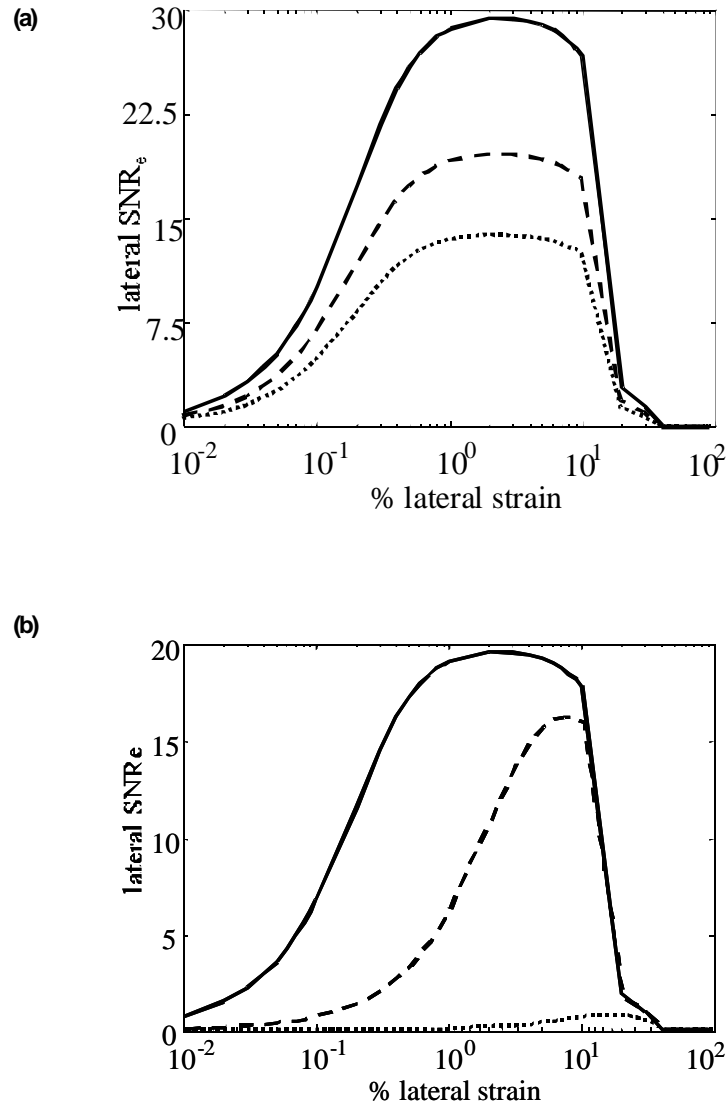


FIG. 5 (a) Dependence on center frequency (MHz): 3.5 (dotted), 5 (dashed), 7.5 (solid). (b) Dependence on sonographic signal-to-noise ratio: 40 dB (100) (dotted), 20 dB (10) (dashed), 0 dB (1) (solid).

the lateral envelope method suffers from less decorrelation noise (at very high strains) where the axial phase method fails and the combination of the two methods can be useful in a dynamic range expansion method.²⁷

2. Verification of LSF with simulations and experiments

In order to verify the theory described above, we generated simulated and experimental LSFs with specific signal processing and ultrasonic parameters. Both simulated and experimental LSFs were generated by plotting SNR_e (calculated using Eq. (21)) vs. the applied axial strain, which, in the case of a homogeneous target, is assumed proportional to the tissue strain.¹⁸ In the case of the simulation, the analytic solution of a homogeneous phantom with stiffness equal to 21 kPa and a Poisson's ratio of 0.495 was used.¹⁰ Axial strains from 0.1%

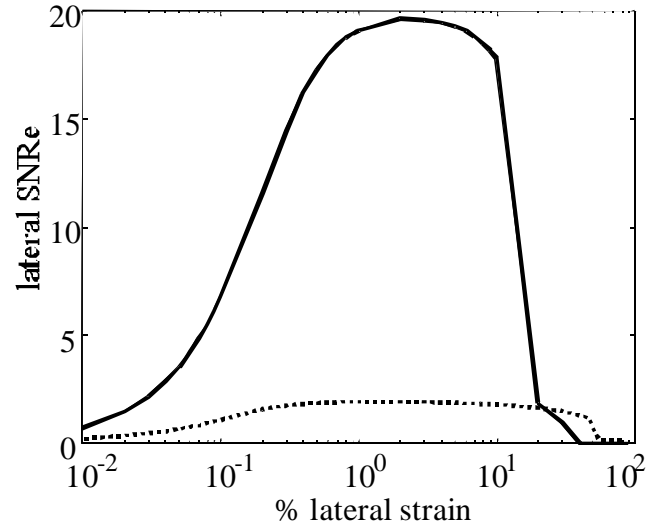


FIG. 6 Theoretical upper bound plots for lateral strain estimation using the lateral envelope (solid) and axial (rf) signal (dotted) for lateral strain estimation.

to 21% were applied in a 2D plane strain model. The pitch was equal to 0.4 mm and the beam width equal to 1 mm, the linear interpolation scheme was equal to 64:1, the center frequency was 5 MHz and the sonographic signal-to-noise ratio (SNR_s) was 40 dB. In the case of the experimental verification, a $90 \times 90 \times 90$ mm³ gelatin phantom containing graphite scatterers (supplied by Dr. Timothy Hall³⁴) was scanned using the Diasonics Spectra scanner with the same ultrasonic parameters as those used in the simulation verification, except for the beam width² being equal to 0.4 mm and SNR_s equal to 30 dB.³⁸ Another difference between simulation and experiment is that motion in the experimental setting was three-dimensional, while in the simulation a plane strain model was assumed. Figure 7 shows the theoretical, simulation and experimental LSFs using the specifications above. Five different renditions of the same homogeneous tissue allowed the generation of the plot with error bars equal to one standard deviation. Figure 8 shows the theoretical, simulation and experimental ASFs before and after correction for the lateral decorrelation. Note how for both high and low strains the simulated ASF after correction further approaches the theoretical upper bound. According to Eq. (22), the lower beamwidth, lower SNR_s and 3D motion decorrelation cause *both* ASFs and LSFs to have lower SNR_e and DR_e in the experimental case (Figs. 7b, 8b) than in the simulation results (Figs. 7a, 8a). However, the most fundamental conclusion to draw from figures 7 and 8 is that both axial and lateral decorrelation expand the dynamic range and increase the overall signal-to-noise ratio at low as well as high strains in *both* axial and lateral strain estimation. Therefore, estimation should be preceded by decorrelation whether estimating strain in 1D, 2D or 3D. Finally, in figure 9, we verify with the same simulations of figures 7 and 8 that the correlation coefficients as associated with the axial and lateral displacement estimates follow the theoretical equations both before and after correction for axial and lateral decorrelation (Eqs. 23 and 24). More importantly, they attain the same level only after decorrelation both at low and high applied strains (i.e., at low and high decorrelations), thereby showing the validity of the assumption in the derivation of Eq. (12) in the case of the decorrelation method. Finally, the lateral decorrelation achieves the same result, i.e., stationarity of the correlation coefficient, as does the lateral confinement shown in Kallel et al.² As a result, the lateral confinement can be avoided in the case where lateral tracking is performed.

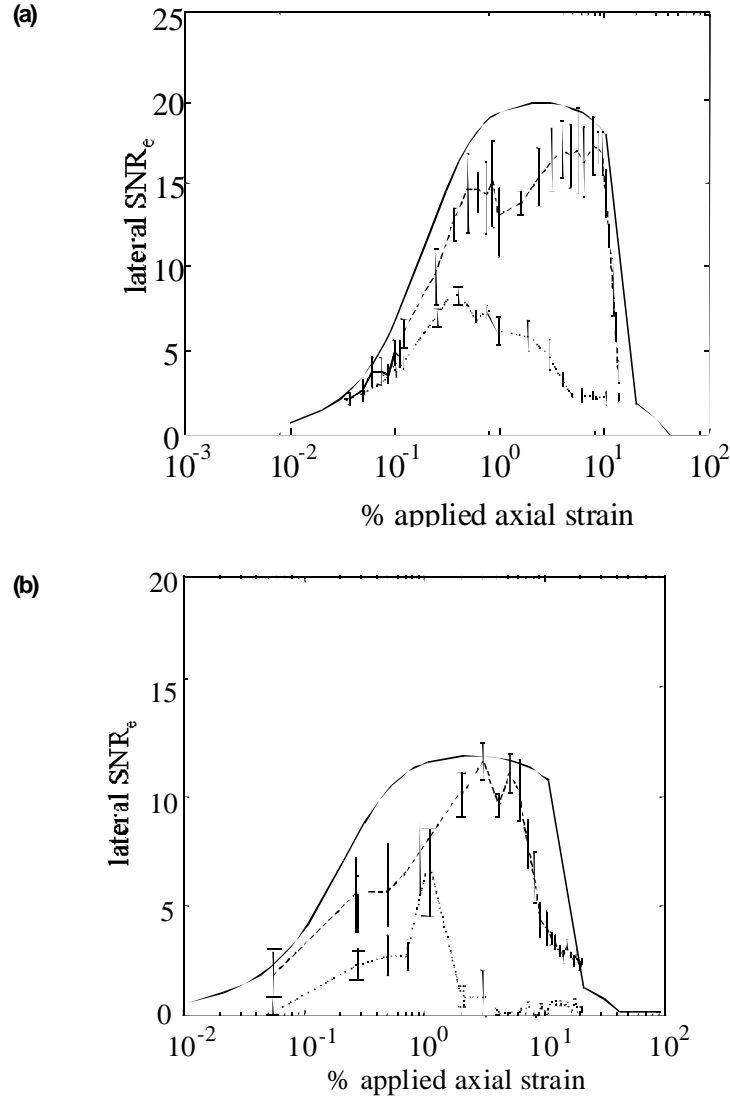


FIG. 7 Theoretical (solid), (a) simulation and (b) experimental Lateral Strain Filters (LSF) with (—) and without (⋯) axial stretching.

2. Theoretical bounds on the estimation of the Poisson's ratio

The standard deviation associated with the Poisson's ratio estimation can be given by

$$\sigma_v = \sigma(\hat{v}) = \sigma \left(\frac{\hat{\epsilon}_l}{\hat{\epsilon}_a} \right) \quad (29)$$

where \hat{v} is the estimated Poisson's ratio and $\hat{\epsilon}_l$ and $\hat{\epsilon}_a$ are the estimated lateral and axial strains, respectively. Bilgen²⁸ has shown that the strain estimates follow a Gaussian distribution. Therefore, the two variables, i.e., axial and lateral strain, could be viewed as jointly Gaussian, and their joint probability density function is equal to²⁹

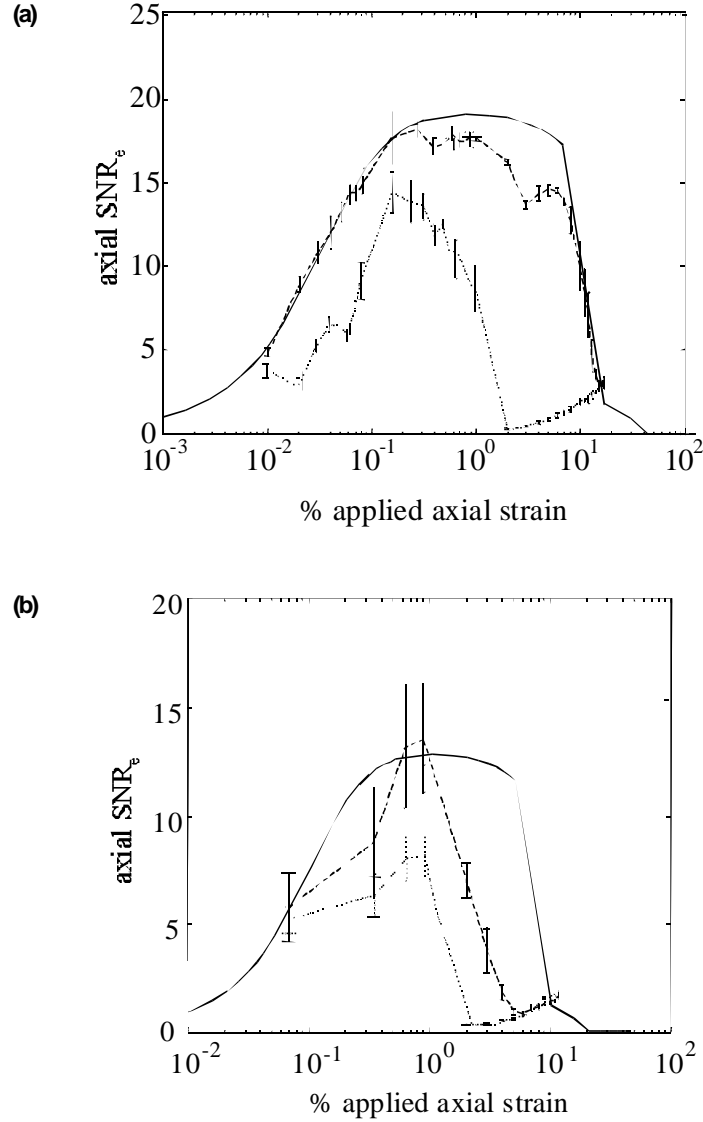


FIG. 8 Theoretical (solid), (a) simulation and (b) experimental Axial Strain Filters (ASF) with (—) and without (---) lateral recorelation.

$$p(\hat{\varepsilon}_a, \hat{\varepsilon}_l) = \frac{1}{2\pi\sigma_a\sigma_l\sqrt{1-\rho^2}} \exp\left[-\frac{1}{2(1-\rho^2)}\left(\frac{\varepsilon_a^2}{\sigma_a^2} - 2\rho\frac{\varepsilon_a\varepsilon_l}{\sigma_a\sigma_l} + \frac{\varepsilon_l^2}{\sigma_l^2}\right)\right] \quad (30)$$

where ρ is the correlation coefficient, and σ_a and σ_l (given by Eq. 19) are the variances characterizing axial and lateral strain estimations, respectively. Their ratio $v = \varepsilon_l/\varepsilon_a$ has a probability density equal to ²⁹

$$p(v) = \frac{\sigma_a\sigma_l\sqrt{1-\rho^2}/\pi}{\sigma_a^2(v - \rho\sigma_l/\sigma_a)^2 + \sigma_l^2(1-\rho^2)} \quad (31)$$

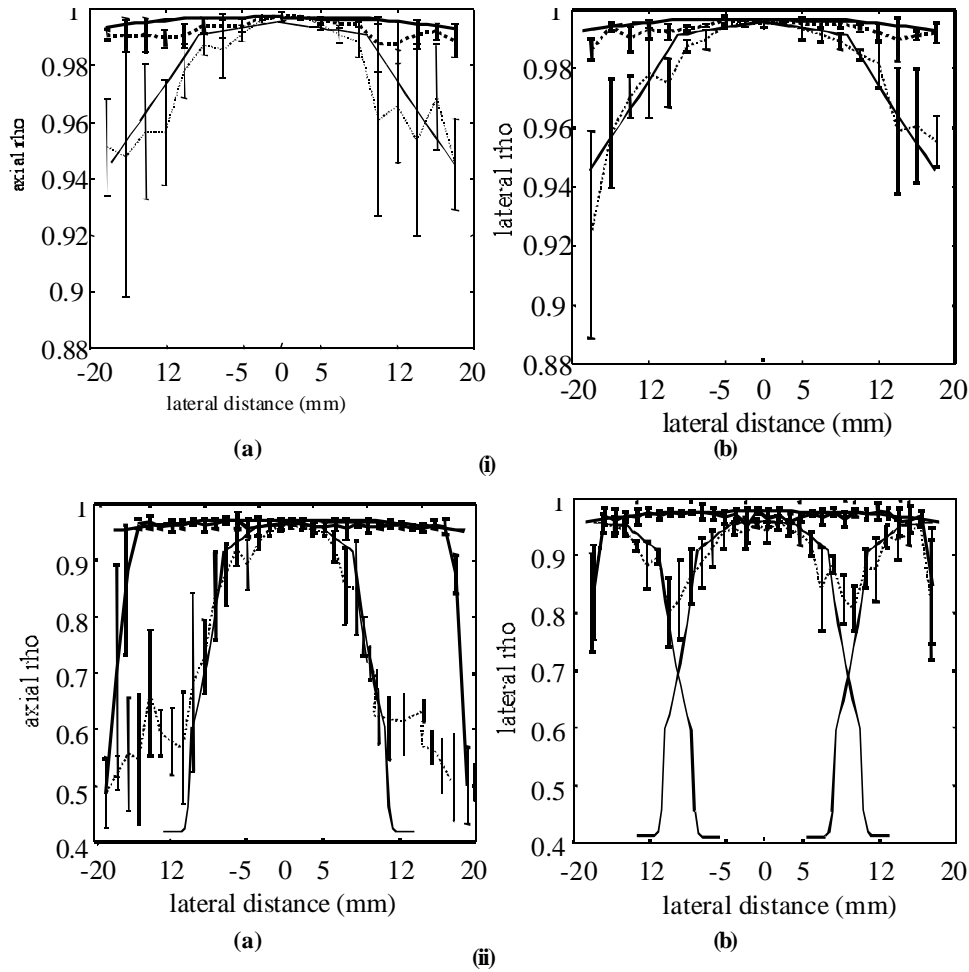


FIG. 9 (a) Theoretical (solid) and simulation (· · ·) axial correlation coefficient and (b) the theoretical (solid) and simulation (—) lateral correlation coefficients before (thin line) and after (thick line) recorrelation (i.e., axial and lateral corrections) at (i) 0.6% and (ii) 3% applied axial strain. Note that, following recorrelation, the axial and lateral correlation coefficients achieve the same level both at low and high applied strains. The decrease in the correlation at the edges in (ii) is due to the fact that motion was higher than the pitch (0.4 mm) and, therefore, could not be tracked (no signal outside the scan). In (ii) b, the signal recorrelates with out tracking towards the edges because the motion is large enough to allow recorrelation with adjacent A-lines.

which satisfies the condition²

$$\int p(v) dv = 1 \quad (32)$$

The variance of the random variable v is defined as

$$\begin{aligned} \sigma^2(v) &= \int (v - \bar{v})^2 p(v) dv \quad (33) \\ &= \int v^2 p(v) dv + \int \bar{v}^2 p(v) dv - 2 \int v \bar{v} p(v) dv \\ &= \int v^2 p(v) dv + \bar{v}^2 \int p(v) dv - 2 \bar{v} \int v p(v) dv \end{aligned}$$

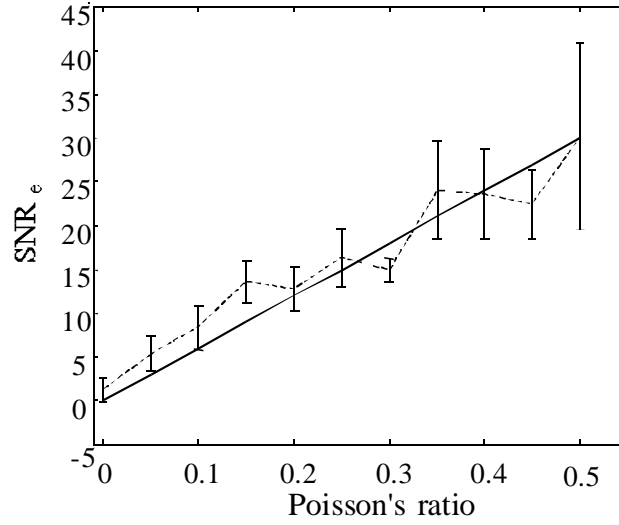


FIG. 10 The Poisson Filter: The theoretical (solid line) SNR_e in the estimation of Poisson's ratio plotted against the true Poisson's ratio for a 2D model verified with simulations (dotted line). Poisson's ratio of 0 denotes a totally incompressible medium while a value of 0.5 corresponds to a totally compressible medium.

$$= \Psi^2(v) - \bar{v}^2 \quad (34)$$

where

$$\Psi^2(v) = \int v^2 p(v) dv \quad (35)$$

denotes the mean-square value and

$$\bar{v} = \int v p(v) dv \quad (36)$$

is the definition of the mean of the random variable v .²¹

Using Eqs. (34) and (36), we derive (using an integral look-up table) the variance in the estimation of the Poisson's ratio given by

$$\sigma^2(\hat{v}) = \left[\frac{\sigma_l \sqrt{I - \rho^2}}{\pi \sigma_a} v + \frac{\rho \sigma_l^2 \sqrt{I - \rho^2}}{\pi \sigma_a^2} \ln \left| \sigma_a^2 v^2 - 2\rho \sigma_l \sigma_a v + \sigma_l^2 \right| \right. \quad (37)$$

$$\left. - \frac{I \left(\frac{\sigma_l}{\sigma_a} \right)^2 \tan^{-1} \left(\frac{\sigma_a v - \rho \sigma_l}{\sqrt{\sigma_a^2 - \rho^2 \sigma_l^2}} \right)}{\pi \left(\frac{\sigma_l}{\sigma_a} \right)^2} \right] - \bar{v}^2$$

where

$$\rho = \rho(\hat{\epsilon}_a, \hat{\epsilon}_l) = \frac{\text{cov}(\hat{\epsilon}_a, \hat{\epsilon}_l)}{\sigma_a \sigma_l} \quad (38)$$

and where $\text{cov}(\hat{\epsilon}_a, \hat{\epsilon}_l)$ is the covariance between the axial and lateral strains. The recorrelation method achieves decoupling of the axial and lateral motions. Therefore, after decoupling, the lateral and axial strains can be considered uncorrelated, i.e., in Eq. (37), $\rho = 0$ and the variance can have a simpler form given by

$$\sigma_v^2 = \sigma^2(\hat{v}) = \frac{\sigma_l}{\pi\sigma_a} \left(v - \frac{\sigma_l}{\sigma_a} \tan^{-1}(\hat{v}) \right) - \bar{v}^2 \quad (39)$$

The upper bound on the Poisson SNR_e , defined by

$$PSNR_e^{UB} = \frac{\bar{v}}{\sigma_v} \quad (40)$$

can then be computed by using the Cramér-Rao Lower Bounds of the axial and lateral variances. Figure 10 was generated using Eqs. (40) and (39) and plots the *Poisson Filter*, i.e., the upper bound of the Poisson SNR_e versus the estimated Poisson's ratio, and corroborates the theoretical result with 2D simulations using the analytical solution of a circular inclusion embedded in an infinite background.³ Note how the performance (measured by SNR_e) improves at higher Poisson's ratios and that the contrast-to-noise ratio should increase with the higher contrast in Poisson's ratios within the target. Since most soft tissues have Poisson's ratios close to 0.5, the Poisson's ratio estimation method applied on soft tissues should yield high quality Poisson's ratio elastograms.

3. CONCLUSIONS

In this study, we developed the theoretical tool for prediction of the performance of lateral (or, transverse) motion estimation. The two estimators considered were the recorrelation method and the lateral envelope method. The recorrelation method corrects the axial signal for axial distortion and tracks it in the lateral direction. The lateral envelope method uses the lateral envelope for lateral tracking. We showed theoretically that the use of the axial signal in estimating lateral motion leads to a significant increase of the signal-to-noise ratio of the lateral strain estimation compared to the estimation using the lateral envelope due to the inherent precision of the axial phase. The performance of lateral tracking estimation increases with the bandwidth, the center frequency, the pitch-to-beamwidth ratio, the sonographic signal-to-noise ratio, the interpolation factor and the degree of recorrelation (or, the correlation coefficient). The performance of the lateral strain estimator using the recorrelation method could be equal to that of the axial strain estimation within a factor of 2-3, assuming that the axial and lateral resolutions are equally close. The theoretical models were verified using 2D simulations and experiments on uniform phantoms and the theoretical lateral as well as axial Strain Filters before and after correction were corroborated. The significance of the recorrelation was demonstrated by showing the increase in the signal-to-noise ratio and dynamic range of the Strain Filters following the recorrelation. Finally, the theoretical Poisson Filter was described that characterizes the estimation of the Poisson's ratio. The higher the Poisson's ratio to be estimated, the higher the signal-to-noise ratio in the estimation and, therefore, in soft tissues where the Poisson's ratio is close to 0.5, the estimator should yield the best results.

ACKNOWLEDGEMENTS

This work was supported in part by NIH Program Project grant P01-CA64597. The authors would also like to express their gratitude to Prof. Periklis Ktonas for his helpful comments on the theoretical derivations. Elisa Konofagou is currently with the Department of Radiology at Brigham and Women's Hospital, Harvard Medical School in Boston, Massachusetts.

APPENDIX A

Derivation of the expression relating the variances in the estimations of the shift and of the magnitude of the peak correlation

In this section, we derive the expression that links the variance in the estimation of the correlation peak magnitude to the variance in estimation of the location of that peak, or estimated shift. The derivation is based on similar derivations obtained by Jensen² and Zagar et al²⁰ but here we expand them and take care of previous errors made.

In order to estimate the variance in both the axial and lateral shifts (and compare them), we need to derive an expression that is general enough to encompass both cases. Both Eqs. (1) and (2) that describe the axial and lateral PSFs can be summarized into the following expression, describing the autocorrelation of a pulse with power spectral density of bandwidth B and center frequency f_0 given by

$$R(\tau) = AB \frac{\sin(2\pi B\tau)}{2\pi B\tau} \cos(2\pi f_0\tau) \quad (\text{A.1})$$

where A is a scaling constant that also compensates for the Gaussian-to-sinc equivalence²⁶ in the case of the axial PSF (Eq. (1)). The lateral PSF is given by Eq. (A.1), since in that case $f_0 = 0$ and $B = 1/b$. By applying a Taylor expansion on both terms of Eq. (A.1), we obtain

$$\hat{R}(\tau) = R(0) \left(\frac{2\pi B\tau - \frac{(2\pi B\tau)^3}{6}}{2\pi B\tau} \right) \left(1 - \frac{(2\pi f_0\tau)^2}{2} \right) \quad (\text{A.2})$$

The variance in the estimation of the correlation peak $R(0)$ is defined as

$$\sigma^2 \{ \hat{R}(0) \} = E \{ [\hat{R}(0) - R(0)]^2 \} \quad (\text{A.3})$$

and from Eq. (A.2) we have

$$\begin{aligned} \sigma^2 \{ \hat{R}(0) \} &= R^2(0) E \left\{ \left[1 - \frac{2}{3} [(\pi B)^2 + 3(\pi f_0)^2] \tau^2 - 1 \right]^2 \right\} \\ &= R^2(0) \left(\frac{2}{3} [(\pi B)^2 + 3(\pi f_0)^2] \right)^2 E \{ \tau^4 \} \end{aligned} \quad (\text{A.4})$$

By assuming that the location τ follows a Gaussian distribution with zero mean and variance $\sigma(\tau)$, we have²¹ and Eq. (A.4) becomes

$$\varepsilon^2 \{ \hat{R}(0) \} = \frac{(2[(\pi B)^2 + 3(\pi f_0)^2])^2}{3} \sigma^4(\tau) \quad (\text{A.5})$$

where

$$\varepsilon^2 \{ \hat{R}(0) \} = \frac{\sigma^2 \{ \hat{R}(0) \}}{R^2(0)}$$

is the definition of the normalized mean-square error.²¹ Eq. (A.5) is essential in the derivation of the Lateral Strain Filter predicting the performance of the lateral tracking and recorrelation method.

APPENDIX B

Derivation of the Lateral Strain Filter for motion tracking using the lateral PSF

The behavior of the upper bound of the SNR_e as a function of lateral tissue strain at a fixed window length forms a bandpass filter in the *strain domain*. The upper bound of the SNR_e is obtained when the total tissue strain (s_t) and the tightest lower bound on the strain estimation standard deviation ($\sigma(\hat{s})_{ZZLB,\rho}$ ⁽¹⁾ the modified Ziv-Zakai lower bound) is used to compute SNR_e given by

$$SNR_e^{UB} = \frac{s_t}{\sigma(\hat{s})_{ZZLB,\rho}} \quad (\text{B.1})$$

Incorporating the modified Ziv-Zakai lower bound (ZZLB) expression for the time-delay estimation (TDE) variance for lateral the lateral envelope from the treatment of Weinstein and Weiss³⁰ and using Eq. (B.1), we obtain

$$\sigma^2(\hat{s})_{ZZLB,\rho} \geq \begin{cases} \frac{(sZ)^2}{6Z\Delta z}, & (2f_{oy}Z/c)SNR_C < \psi \\ \text{Threshold} & \psi < (2f_{oy}Z/c)SNR_C < \beta \\ \sigma^2(\hat{s})_{CRLB,\rho} = \frac{2\sigma^2(\hat{d})_{CRLB,\rho}}{Z\Delta z}, & \beta < (2f_{oy}Z/c)SNR_C \end{cases} \quad (\text{B.2})$$

⁽¹⁾The lower bounds on the strain estimation variance are denoted with an additional subscript ρ to indicate that these variances are computed for partially correlated signals. These lower bounds converge to the classical bounds when $\rho = 1$.

where SNR_c represents the composite signal-to-noise ratio, and β and ψ are the thresholds (Eq. (B.2)). Equation (B.2) illustrates the two distinct operating regions for $\sigma(\hat{s})_{ZLB,\rho}$, depending on the value of $(2f_\alpha Z/c)SNR_c$. A distinct threshold region is observed between the Cramér-Rao lower bound^{31,32} (CRLB) and the constant variance level. The variance increases exponentially in this threshold region.³³ Accurate estimation of the strain is possible only within the CRLB. Since the lateral envelope contains no phase information, the Barankin bound (increased variance level due to peak-hopping errors caused by the presence of phase ambiguities in RF signals) is absent.

Expression for the Cramér-Rao lower bound using the lateral envelope

In this section, we derive a CRLB expression for the variance of the displacement estimator using the lateral envelope. The following derivation is based on the treatment for partially correlated signals by Walker and Trahey.³³ The CRLB can be achieved only for zero-strain. However, the expression of the CRLB derived by Walker and Trahey³³ increases the bound on the variance to a more achievable level by incorporating the effect of signal decorrelation. The lower bound on the variance of the jitter for any unbiased displacement estimator is given by Carter³⁴ as

$$\sigma^2(\hat{d})_{CRLB,\rho} \geq \frac{1}{\frac{2Z}{c} \int_{-\infty}^{+\infty} (2\pi k)^2 \frac{C_{r_1 r_2}(k)}{1 - C_{r_1 r_2}(k)} dk} \quad (B.3)$$

where Z is the cross-correlation window length, c is the speed of sound in tissue, k is the wave number, and $C_{r_1 r_2}(k)$ is the magnitude-squared coherence function defined as

$$C_{r_1 r_2}(k) = \left| \frac{G_{r_1 r_2}(k)}{\sqrt{G_{r_1 r_1}(k) G_{r_2 r_2}(k)}} \right|^2 \quad (B.4)$$

where $G_{r_1 r_2}(k)$ is the cross power spectrum of the pre- and post-compression signals ($r_1(z)$ and $r_2(z)$ respectively), while $G_{r_1 r_1}(k)$ and $G_{r_2 r_2}(k)$ are their respective autospectra. Analytical expressions for the cross- and auto-power spectra have been derived by Walker and Trahey³³ for partially correlated signals, and are given by

$$\begin{aligned} G_{r_1 r_2}(k) &= \rho \vartheta_{e_1} \vartheta_{e_2} G_{ee}(k) \\ G_{r_1 r_1}(k) &= \vartheta_{e_1}^2 G_{ee}(k) + \vartheta_{n_1}^2 G_{nn}(k) \\ G_{r_2 r_2}(k) &= \vartheta_{e_2}^2 G_{ee}(k) + \vartheta_{n_2}^2 G_{nn}(k) \end{aligned} \quad (B.5)$$

where ϑ_{e_1} , ϑ_{e_2} , ϑ_{n_1} , ϑ_{n_2} are the root mean squared (rms) amplitudes of $e_1(z)$, $e_2(z)$, $n_1(z)$, and $n_2(z)$ respectively, ρ is the correlation coefficient between $e_1(z)$ and $e_2(z)$, $G_{ee}(k)$ and $G_{nn}(k)$ are functions representing the shape of the signal and noise power spectra scaled such that their integral is unity. In addition, the cross correlation between $e_1(z)$ and $e_2(z)$ is assumed to have the same shape as the auto-correlation of either signal, scaled to account for signal decorrelation and signal amplitude. The results in Eq. (B.4) are substituted into Eq. (B.3) to obtain a lower bound on the performance of the displacement estimator.

To obtain a closed form solution, bandlimited spectra are assumed for both the signal and the noise and spanning the same frequency spectrum. For the lateral PSF (sinc squared), we obtain a triangular spectrum

$$G_{ee}(k) = G_{nn}(k) = \begin{cases} 1 - \left| \frac{k}{D} \right| & -f_{oy} \leq k \leq f_{oy} \\ 0 & \text{elsewhere} \end{cases} \quad (\text{B.6})$$

where $f_{oy} = \lambda z/D$, for center wavelength λ , range z and aperture size D . The equivalent square spectrum for the sinc squared function is given by

$$G_{ee}(k) = G_{nn}(k) = \begin{cases} \frac{1}{f_{oy}} & -f_{oy}/2 \leq k \leq f_{oy}/2 \\ 0 & \text{elsewhere} \end{cases} \quad (\text{B.7})$$

Substituting Eq. (B.6) into Eq. (B.7), and computing the lower bound on the displacement estimation variance we obtain

$$\sigma^2(\hat{d})_{CRLB,\rho} \geq \frac{3c}{2\pi^2 X f_{oy}^3} \left[\frac{1}{\rho^2} \left(1 + \frac{1}{SNR_1^2} \right) \left(1 + \frac{1}{SNR_2^2} \right) - 1 \right] \quad (\text{B.8})$$

where $SNR_1 = \vartheta_{e_1} / \vartheta_{n_1}$ and $SNR_2 = \vartheta_{e_2} / \vartheta_{n_2}$ are the electronic (sonographic) signal to noise ratios in the pre- and post-compression signals. Generally $SNR_1 \cong SNR_2$, leading to a simplification of the expression for variance of the displacement estimator, that is given by

$$\sigma^2(\hat{d})_{CRLB,\rho} \geq \frac{3c}{2\pi^2 X f_{oy}^3} \left[\frac{1}{\rho^2} \left(1 + \frac{1}{SNR^2} \right)^2 - 1 \right] \quad (\text{B.9})$$

This expression predicts the lower bound on the jitter errors incurred while estimating the displacement between two partially correlated lateral envelopes corrupted by electronic noise. The correlation coefficient used in Eq. (B.9) varies with applied strain and is itself also dependent on the window length (X) used to compute the normalized cross-correlation function. An expression for the effective lateral correlation coefficient that depends on tissue strain, lateral envelope decorrelation and the finite length window is derived in the next section.

Expression for the effective lateral correlation coefficient.

The following expression for the correlation coefficient is based on the treatment of Bilgen and Insana³⁵ and is modified in this work for lateral envelopes. For the tissue and ultrasound system model described in section 4.5, the cross-correlation function, between the pre- and the post-compression signals is calculated using

$$\langle \hat{\Gamma}_{12}(z') \rangle = \left\langle \frac{1}{Z} \int_{-Z/2}^{Z/2} r_1(z - z') r_2(z) dz \right\rangle \quad (\text{B.10})$$

where the square bracket $\langle \cdot \rangle$ denotes the ensemble average, and z' denotes the shift variable. The autocorrelation functions $\hat{\Gamma}_{11}(tz)$ for the pre- and $\hat{\Gamma}_{22}(z')$ for the post-compression signals are also computed. The effective correlation coefficient can be written as

$$\rho = \frac{\hat{\Gamma}_{12}(0)}{\sqrt{\hat{\Gamma}_{11}(0)\hat{\Gamma}_{22}(0)}} = \rho_{PEAK} \times M \quad (\text{B.11})$$

The term ρ_{PEAK} represents the peak correlation coefficient due to the two-point ensemble averaging (Bilgen and Insana³³). The peak correlation coefficient for lateral envelopes can be expressed as follows

$$\rho_{PEAK} = \frac{\left(L_f^2 + L_h^2\right)^{1/4} \left(L_f^2 + a^2 L_h^2\right)^{1/4}}{\eta} \quad (\text{B.12})$$

where

$$\eta^2 = L_f^2 + \frac{1+a^2}{2} L_h^2$$

The factor M in Eq. (B.11) is due to the finiteness of the window length and is given by the integral

$$M = \frac{1}{Z} \int_{-Z/2}^{Z/2} \exp\left(-\frac{((1-a)z)^2}{4\eta^2}\right) dz \quad (\text{B.13})$$

For zero strain, $s=0$, $a=1$ and one can show that $M=1$ in the limit. Non zero strains, on the other hand, yield $M<1$ and consequently reduces the correlation coefficient ρ .

REFERENCES

1. Ophir, J., Céspedes, I., Ponnekanti, H., Yazdi, Y. and Li, X., Elastography: a quantitative method for imaging the elasticity of biological tissues, *Ultrasonic Imaging* 13, 111-134 (1991).
2. Kallel, F., Varghese, T., Ophir, J. and Bilgen, M. The nonstationary strain filter in elastography, Part II: Lateral and elevational decorrelation, *Ultrasound Med. Biol.* 23, 1357-1369 (1997).
3. Konofagou, E.E. and Ophir, J., A new elastographic method for estimation and imaging of lateral strains, corrected axial strains and poisson's ratios in tissues, *Ultrasound Med. Biol.* 24, 1183-1199 (1998).
4. Varghese, T., Ophir, J. and Céspedes, E. I., Noise reduction in elastography using temporal stretching with multicompression averaging, *Ultrasound Med. Biol.* 22, 1042-1053 (1996).
5. Konofagou E.E., Estimation and imaging of 3D motion and Poisson's ratio in elastography, *Ph.D. dissertation* (University of Houston, 1999).
6. Céspedes, I. and Ophir, J., Reduction of image noise in elastography, *Ultrasonic Imaging* 15, 89-102 (1993).
7. Sarvazyan, A.P., Low frequency acoustic properties of biological tissues, *Mech. Polymers* 4, 691-695 (1975).

8. Skovoroda, A.R., Emelianov, S.Y., Lubinski, A.M., Sarvazyan, A.P. and O'Donnell, M., Theoretical analysis and verification of ultrasound displacement and strain imaging. *IEEE Trans. Ultras., Ferroel. Freq. Control* 41, 302-313 (1994).
9. Sumi, C., Suzuki, A. and Nakayama, K., Estimation of shear modulus distribution in soft tissue from strain distribution. *IEEE Trans. Biomed. Eng.* 42, 193-212 (1995).
10. Kallel, F., Bertrand, M. and Ophir, J., Advances in tissue elasticity reconstruction using linear perturbation method, in *Acoustical Imaging*, pp. 267-277, J.P. Jones, ed. (Plenum Press, New York, 1996).
11. Mridha, M., Ödman S. Noninvasive method for assessment of subcutaneous edema, *Med. Biol. Eng. Comp.* 24, 393-398 (1986).
12. Fung, Y.C., Connecting in cremental shear modulus and Poisson's ratio of lung tissue with morphology and theology of microstructure, *Biorheology* 26, 279-289 (1989).
13. Jurvelin, J.S., Buschmann, M.D. and Hunziker, E.B., Optical and mechanical determination of Poisson's ratio of adult bovine humeral articular cartilage, *J. Biomech.* 30, 235-241 (1997).
14. Lubinski, A.M., Emelianov, S.Y., Raghavan, K.R., Yagle, A.E., Skovoroda, A.R. and O'Donnell, M., Lateral displacement estimation using tissue incompressibility, *IEEE Trans. Ultras. Ferroel. Freq. Control* 43, 247-156 (1996).
15. Walker W.F. and Trahey G.E. A Fundamental Limit on the performance of correlation-based phase correction and flow correction and flow estimation techniques, *IEEE Trans. Ultras. Ferroel. Freq. Cont.* 41, 644-654 (1994).
16. Wagner, R.F., Smith, S.W., Sandrik, J.M. and Lopez, H., Statistics of speckle in ultrasound B-Scans. *IEEE Trans. Sonics Ultras.* 30, 156-163 (1983).
17. Bonnefous, O., Measurement of the complete (3D) velocity vector of blood flows, in *Proc. IEEE Ultras. Symp.*, pp. 795-799 (1988).
18. Varghese, T. and Ophir, J. A theoretical framework for performance characterization of elastography: the Strain Filter, *IEEE Trans. Ultras. Ferroel. Freq. Cont.* 44, 164-172, (1997).
19. Burckhardt, C. B., Speckle in ultrasound B-Mode scans, *IEEE Trans. Sonics Ultras.* 25, 1-6 (1978).
20. Zagar B.G., Fornaris R.J. and Ferrara K.W., Ultrasonic mapping of the microvasculature, signal alignment, *Ultras. Med Biol.*, 809-824 (1998).
21. Bendat J.S. and Piersol, A.G., *Random Data, Analysis and Measurement Procedures*, (John Wiley & Sons, New York, 2nd edition, 1986).
22. Jensen, J.A. *Estimation of Blood Velocities Using Ultrasound* (Cambridge University Press, Cambridge, U.K., 1996).
23. Mallart, R. and Fink, M., The Van Cittert-Zernike theorem in pulse echo measurements, *J. Acoust. Soc. Amer.* 90, 2718-2727 (1991).
24. Ng, G.C., Worrell, S.S., Freiburger, P.D. and Trahey, G.E., A comparative evaluation of several algorithms for phase aberration correction, *IEEE Trans. Ultras., Ferroel. Freq. Control* 41, 631-643 (1994).
25. Céspedes, I., Insana, M. and Ophir, J. Theoretical bounds on strain estimation in elastography, *IEEE Trans Ultras., Ferroel. Freq. Control* 42, 969-972 (1995).
26. Bilgen, M. and Insana, M.F. Error analysis in acoustic elastography, II. Strain estimation and SNR analysis, *J. Acoust. Soc. Am.* 101, 1147-1154 (1997).
27. Konofagou, E.E., Ophir, J., Kallel, F. and Varghese, T., Elastographic dynamic range expansion using variable applied strains, *Ultrasonic Imaging* 19, 145-166 (1997).
28. Bilgen, M., Target detectability in acoustic elastography, *IEEE Trans. Ultras., Ferroel. Freq. Control* 46, 1-6 (1999).
29. Papoulis A., *Probability, Random Variables and Stochastic Processes* (McGraw Hill, New York, 1st edition, 1965).
30. Weinstein, E. and Weiss, A., Fundamental limitations in passive time delay estimation – Part I, Narrow-band systems, *IEEE Trans. Acoust, Speech, Sig. Proc.* 31, 472-485 (1983).
31. Carter, G.C., Coherence and time delay estimation, *IEEE Proc.* 75, 236-255 (1987).
32. Walker, W.F. and Trahey, G.E., A fundamental limit on delay estimation using partially correlated speckle signals, *IEEE Trans. Ultras. Ferroel. Freq. Cont.* 42, 301-308 (1995).

33. Bilgen, M. and Insana, M.F., Deformation models and correlation analysis in elastography, *J. Acoust. Soc. Am.* 99, 3212-3224 (1996).
34. Hall, T.J., Bilgen, M., Insana, M.F. and Krouskop, T.A., Phantom materials for elastography, *IEEE Trans. Ultrason. Ferroel. Freq. Cont.* 44, 1355-1365 (1997).